

Geophysical Research Letters®



RESEARCH LETTER

10.1029/2024GL108421

Mixing, Water Transformation, and Melting Close to a Tidewater Glacier

Key Points:

- Entrainment into the buoyant plume drives ~65% of fjord vertical overturning circulation
- Intense turbulent mixing in the horizontal spreading phase of the plume drives the remaining ~35%
- 95%–98% of the heat in the rising plume short-circuits the glacier, to be redistributed into glacial proximal waters by horizontal mixing

Supporting Information:

Supporting Information may be found in the online version of this article.

Correspondence to:

M. E. Inall,
Mark.Inall@sams.ac.uk

Citation:



Inall, M. E., Sundfjord, A., Cottier, F., Korte, M.-L., Slater, D. A., Venables, E. J., & Coogan, J. (2024). Mixing, water transformation, and melting close to a tidewater glacier. *Geophysical Research Letters*, 51, e2024GL108421. <https://doi.org/10.1029/2024GL108421>

Received 19 JAN 2024

Accepted 9 JUL 2024

Author Contributions:

Conceptualization: Mark E. Inall, Arild Sundfjord, Finlo Cottier
Data curation: Mark E. Inall, Arild Sundfjord
Formal analysis: Mark E. Inall, Arild Sundfjord, Marie-Louise Korte, Emily J. Venables
Funding acquisition: Mark E. Inall, Finlo Cottier
Investigation: Mark E. Inall, Arild Sundfjord, Emily J. Venables, James Coogan
Methodology: Mark E. Inall, Arild Sundfjord, Finlo Cottier
Project administration: Mark E. Inall
Resources: Mark E. Inall, Emily J. Venables
Software: Mark E. Inall, Donald A. Slater, James Coogan

Mark E. Inall¹ , Arild Sundfjord² , Finlo Cottier¹ , Marie-Louise Korte¹ , Donald A. Slater³ , Emily J. Venables⁴, and James Coogan¹

¹SAMS UHI, Oban, Scotland, ²Norsk Polarinstitut, Tromsø, Norway, ³University of Edinburgh, Edinburgh, Scotland, ⁴UiT The Arctic University of Norway, Tromsø, Norway

Abstract Marine-terminating glacier fjords play a central role in the transport of oceanic heat toward ice sheets, regulating their melt. Mixing processes near glacial termini are key to this circulation but remain poorly understood. We present new summer measurements of circulation and mixing near a marine-terminating glacier with active sub-glacial discharge. 65% of the fjord's vertical overturning circulation is driven by the buoyant plume, however we newly report intense vertical and horizontal mixing in the plume's horizontal spreading phase, accounting for the remaining 35%. Buoyant plume theory supports 2%–5% of total glacial melt. Thus, most of the heat associated with vertical overturning short-circuits the glacial front. We find however that turbulence in the horizontal spreading phase redistributes the short-circuited heat back into the surface waters of the near-glacial zone. Our findings highlight the need for further research on the complex mixing processes that occur near the glacier terminus.

Plain Language Summary Melting of glacial ice is the single largest contributor to global sea-level rise. Many glaciers flow into the ocean where the near-vertical ice wall is bathed in relatively warm sea water. Freshwater from ice surface melting seeps down through cracks and crevasses in the glacier to be discharged at the base of the ice wall, many tens to hundreds of meters below the sea surface. This fresh water rises from the depths as a highly turbulent plume, drawing in and pushing upwards the surrounding seawater, eventually spreading horizontally as a mixture of fresh discharge and mixed-in seawater. Few measurements exist in the dangerous zone where iceberg often calve. Using data from a robotic platform we show that the vertical rise and the horizontal spreading of fresh water both play important roles in the total ocean-induced melting of the glacial face in this type of system.

1. Introduction

Ice mass loss contributes to both sea-level rise and ocean surface freshening, with ice/ocean interaction taking place near marine terminating glaciers (MTGs). Ocean-driven melting and calving both contribute significantly to ice loss for many MTGs (Davison et al., 2020; Kneib-Walter et al., 2021; Moyer et al., 2019), but their relative contributions are rarely constrained (Sutherland et al., 2019). The majority (~90%) of MTG surface meltwater percolates through crevasses to the glacial base from where it discharges into the fjord, typically at grounding line depth, rising as buoyant plumes (BPs), which entrain ambient fjordic water and may locally increase glacier front melting. The relative contributions to total melt of BP-induced melting versus ambient ocean-induced melting is poorly constrained. Recent work suggests a far greater role for ambient melting than that predicted by plume theory (Bendtsen et al., 2015; Jackson et al., 2020). Total submarine melting may however be increased by near-frontal dynamics driven by subglacial discharge (Cusack et al., 2023; Jackson et al., 2022). Total ice loss of some MTGs correlates strongly with ocean temperature within a melt season (Luckman et al., 2015), and ice sheet mass loss on longer time scales exhibits sensitivity to ocean conditions (Murray et al., 2010). Therefore, heat delivery processes from ocean to glacial terminus mediated by fjord circulation play an important role in calving and melting rates on all time scales. The greatest uncertainties lie in the region where plumes can both drive and interact with fjord circulation and is the focus of this study.

Fjord circulation can be decomposed into a laterally averaged vertical circulation cell and depth- or layer-averaged horizontal circulation cells; the terms adopted here are vertical overturning and lateral circulation, respectively. In wide fjords, those with width W exceeding one Rossby radius \mathcal{R} , lateral circulation is typically as strong as vertical overturning (Carroll et al., 2017; Zhao et al., 2021). The extent to which lateral and vertical circulation interact has been investigated in modeling studies (Carroll et al., 2017; Zhao et al., 2021, 2022). In

© 2024. The Author(s).

This is an open access article under the terms of the [Creative Commons Attribution License](https://creativecommons.org/licenses/by/4.0/), which permits use, distribution and reproduction in any medium, provided the original work is properly cited.

Supervision: Mark E. Inall
Validation: Mark E. Inall, Donald A. Slater
Visualization: Mark E. Inall, Marie-Louise Korte, James Coogan
Writing – original draft: Mark E. Inall
Writing – review & editing: Mark E. Inall, Arild Sundfjord, Finlo Cottier, Marie-Louise Korte, Donald A. Slater

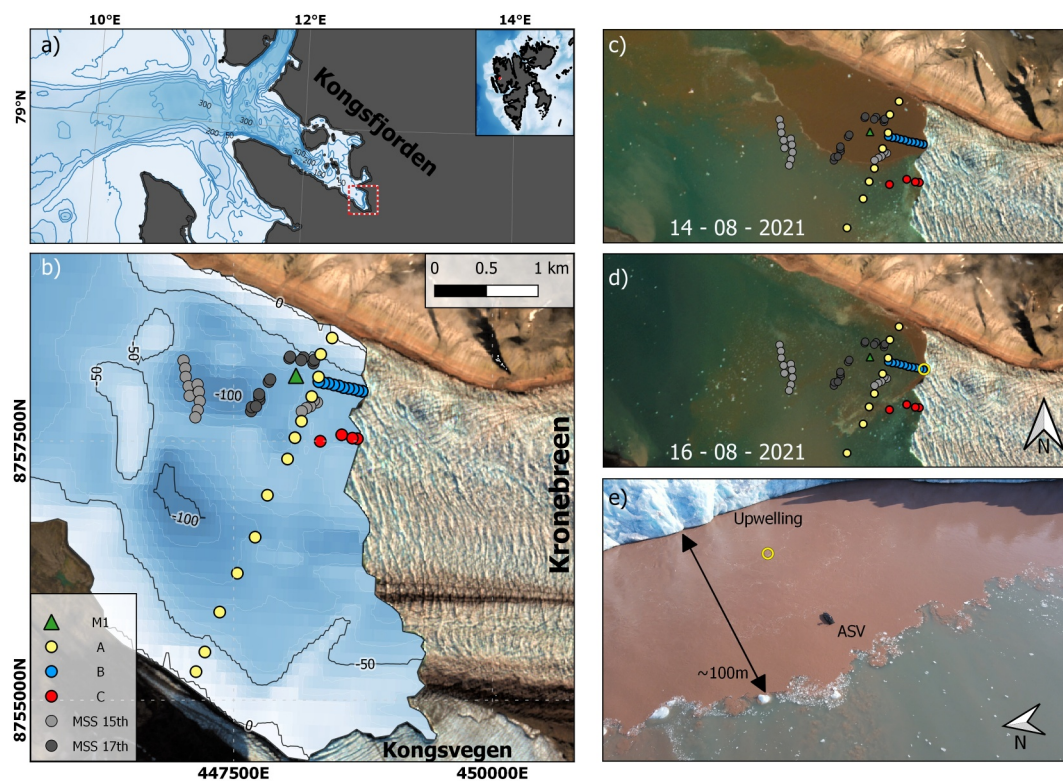


Figure 1. Location map. (a) Kongsfjorden, west Svalbard (north of mainland Norway). (b) Observational locations superimposed on bathymetric contours, overlaid with Sentinel 2 image. Symbols mark Conductivity, Temperature, Depth/ MSS Sections A–C, as indicated in key. Axes in UTM easting and northing. (c, d) Visible-band Sentinel-2 images from 14 and 16 August 2021. (e) Drone footage showing Autonomous Surface Vehicle Apherusa near the upwelling (16 August), open yellow circle as located in panel (d).

Zhao et al. (2021) no mixing processes are present except within a rising discharge plume, whilst in Carroll et al. (2017) vertical mixing occurs between layers, with a consequential 26% increase in vertical overturning. Another study proposes scaling laws relating overturning and lateral circulation to subglacial discharge rate, noting positive feedback pathways to glacial melt (Zhao et al., 2022). No observational studies have addressed the interplay between vertical overturning, vertical mixing, and lateral circulation. We present new observations of turbulent mixing in the lateral spreading phase (hereafter, plume pool) of a subglacial discharge plume, associated vertical heat fluxes and effective horizontal transports necessary to close heat, salt, and volume budgets. These analyses are placed in the context of observationally-quantified vertical overturning and lateral circulation, and the combined predicted effects on melt estimated using a BP model (Slater et al., 2016).

2. Observations and Data Processing

Observations are from Kronebreen glacier and Kongsfjorden ($W \approx 5 \text{ km} > R \approx 3.3 \text{ km}$) West Svalbard, between 14 and 21 August 2021 during a period of light winds (Figure 1) and comprised: a vessel-tethered TRDI 600 kHz Acoustic Doppler Current Profiler (ADCP); a MSS90 Conductivity, Temperature, Depth (CTD) and shear microstructure sonde (Prandke & Stipps, 1998); an FSI Castaway CTD deployed from *RV Teisten* and a Seabird SBE19+ CTD with an optical backscatter turbidity sensor deployed from the Autonomous Surface Vehicle (ASV) *Apherusa* (Figure 1, Inall, 2023; Sundfjord et al., 2024).

Twelve stations with spacing of $\sim 275 \text{ m}$ taken from *Teisten* on 16 August form cross-fjord CTD/ADCP Section A, parallel to and approximately 400 m from the glacier front. Two ASV CTD Sections B (16 August) and C (17 August) run from the glacier face to Section A. Within Section B there is a visible plume pool, not so on Section C. The ADCP was deployed at the ocean surface ($z = 0.4 \text{ m}$) beneath a buoy loosely tethered to *RV Teisten*. Data were collected to from 2 to $\sim 50 \text{ m}$ into 1 m bins with 10 s ensemble averaging, standard error per ensemble was

0.97 cm s⁻¹. Ensembles were motion-corrected using a GPS sampling at 1 s attached to the ADCP, and further time-averaged over the duration of each station (30, 10-s ensembles per station), reducing station velocity error to 0.18 cm s⁻¹. Additionally, a total of 37 MSS90 casts were taken near Section A on 15 and 17 August providing profiles of TKE dissipation, $\epsilon(z)$, and vertical turbulent heat flux following Sundfjord et al. (2007) with a vertical resolution of 1 m centered from 0.5 m (CTD) or 2 m (ϵ) below the surface to 0.6 m above the bed.

ADCP data were rotationally aligned with Section A, and ADCP and CTD data linearly interpolated onto a common grid ($dz = 1$ m, $dy = 100$ m), and extrapolated to the surface, sides and bed using a range of techniques for error estimation (Jackson & Straneo, 2016) (see Supporting Information S1). In the presented figures, CTD data were extrapolated to the sides using nearest constant values, linearly to the bed and no extrapolation to the surface. ADCP data were treated similarly at the sides, and linearly extrapolated to the surface. Geostrophic velocity shear was calculated using CTD data, interpolated onto the common grid then integrated downwards from the deepest ADCP bin to the seabed, determined using high resolution bathymetry (Lindbäck et al., 2018).

3. Analysis

3.1. Aerial View

The surface expression of vigorous and persistent (Howe et al., 2019) subglacial discharge was visible as a plume pool in satellite and drone imagery (Figures 1c–1e; Copernicus, 2023; ESA, 2023). On 16 August the plume pool was capped by a fresh layer of less turbid water (Figure 1d). An area of weakly-turbid surface water to the south originated from a land-terminating section of Kongsvegen glacier. Maximal surface flow near the upwelling center of the plume pool (Figure 1e) was >2 ms⁻¹, derived from ASV speed-through-water and drone video analysis.

3.2. Section A

Warmest waters on Section A were located below the plume pool, and the coldest below ~ 45 m ($\sigma_\theta > 27.25$) where flow was weak. Section A was salt stratified, strongest above and below warm Atlantic-origin water found between ~ 15 and ~ 50 m (Figure 2a). Here stratification was weak with extensive regions of marginal stability, defined as Richardson Number $Ri = N^2/(\partial U/\partial z)^2 < 1$ (Figure 2b). Within the plume pool, outflow away from glacier peaked at ~ 30 cm s⁻¹ in a core situated at ~ 8 m above a weaker inflow of a few cm s⁻¹, with fastest inflow of ~ 6 cm s⁻¹ recorded at ~ 20 m (Figure 2b), offset to the south of the peak surface outflow. The stratified plume pool was vertically sheared above and below its core, and highly turbulent throughout. Turbulence profiles were bootstrapped to give daily $\epsilon(z)$ profiles with 95% confidence limits (Figure 3b). A transition at $\sigma_\theta = 26.4$ (~ 10.4 m depth) separates quiescent deeper waters from the highly turbulent plume pool. 15th August exhibited more turbulent, higher density surface waters than the 17th, when a fresher layer capped the plume pool.

A good measure of the overall strength of the lateral circulation is the maximum value of the depth integrated lateral stream function, $\psi_{full}^h(x)_{max} \sim 450$ m³ s⁻¹. However, the velocity normal to Section A exhibits a checkerboard pattern, consistent with two counter-rotating lateral circulation cells. In both upper ($\sigma_\theta < 26$, $z < 10$ m) and lower cells ($26.65 < \sigma_\theta < 26.9$, ~ 15 to ~ 25 m) flows toward the glacier are associated with warmer waters. Layer-wise velocity integrations (from south to north, Figure 2c) show the two lateral cells, $\psi_{upper}^h(x)$ and $\psi_{lower}^h(x)$, to be of similar strength (see Supporting Information S1). The two layers “communicate” through vertical overturning driven by the sub-glacial discharge. The vertical overturning stream function (width-integrated), $\psi^v(\sigma)$, is computed in density-space (Figure 3a), rather than depth-space, to reveal the water property transformation between Section A and the glacier. $\psi^v(\sigma)$ has a single maximum, comparable in strength to the lateral cells, of $\psi^v(\sigma)_{max} = 651 \pm 62$ m³ s⁻¹ at $\sigma_\theta = 25.65$ (~ 7 m). Thus, denser waters ($\sigma_\theta = 27.15$ to 25.65 , or ~ 50 to ~ 7 m) are transformed into lighter ones ($\sigma_\theta = 25.65$ to 24.4 , or ~ 7 – 2 m) at a rate of 651 ± 62 m³ s⁻¹. Transport toward the glacier increases between $\sigma_\theta = 27.15$ and 25.9 , consistent with entrainment of ambient fjord waters into the rising plume. Decreasing transport shallower than $\sigma_\theta = 25.65$ corresponds physically to the spreading plume pool. The negative cumulative transport $\psi^v(\sigma_{min}) = -33 \pm 65$ m³ s⁻¹ arises from runoff and subglacial discharge flowing away from the glacier and through Section A as a net negative flow across the section. Although a realistic value for summer freshwater discharge (Sundfjord et al., 2017; Svendsen et al., 2002; Tverberg et al., 2019), the error is large since only volume conservation is invoked. Following Jackson et al. (2022) we additionally calculate the total freshwater input into the fjord, $Q_{fw} = 30 \pm 1.6$ m³ s⁻¹ using

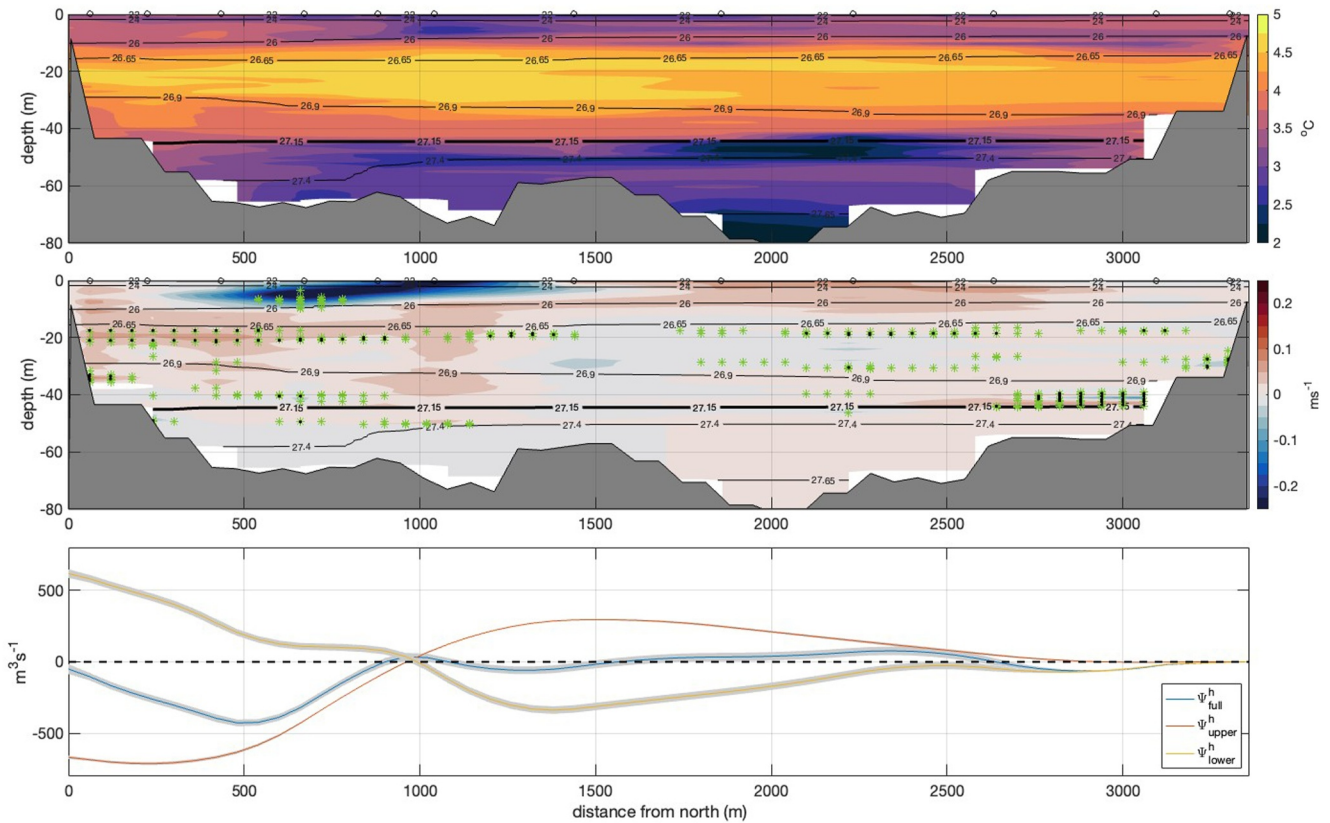


Figure 2. Section A. (a) Conservative temperature with σ_θ overlay from MSS-CTD. $\sigma_\theta = 27.15$ marks the lower integration limit for vertical overturning. Open circles indicate Station A positions; (b) Along-fjord velocity from Acoustic Doppler Current Profiler (positive toward glacier), $R_i < 1$ and $R_i < \frac{1}{4}$ green and black markers; (c) lateral circulation stream function (integrated from south to north) for full water column and upper ($\sigma_\theta < 26$) and lower ($26.65 < \sigma_\theta < 26.9$) layers. Horizontal axis is distance in meters from the northern shoreline.

combined conservations of volume, heat, and salt (see Supporting Information S1 for methods including error estimation). Q_{fv} into the control volume is positive and, if storage is zero, results in a transport away from the glacier (negative) comprising $Q_M = 4.9 \text{ m}^3 \text{ s}^{-1}$ (submarine meltwater) and $Q_R = 25.1 \text{ m}^3 \text{ s}^{-1}$ (the residual), assumed to be predominantly subglacial discharge. $\psi^r(\sigma)_{\text{max}} = 651 \pm 62 \text{ m}^3 \text{ s}^{-1}$ therefore reveals a twenty-six-fold increase in water mass transformation rate relative to plume discharge rate ($Q_R = 25.1 \text{ m}^3 \text{ s}^{-1}$), consistent with the other observations of subglacial discharge plumes (Jackson et al., 2020; Mankoff et al., 2016).

3.3. Buoyant Plume Model

A BP model (Slater et al., 2016) was implemented using $Q_R = 25.1 \text{ m}^3 \text{ s}^{-1}$, a cavity width of 70 m at the grounding line depth of 50 m and entrainment of water with $T(z)$ and $S(z)$ from Section A. The cavity width was selected (as in Jackson et al., 2017) to ensure the plume entrainment matched the observed overturning up to $\sigma_\theta = 26.4$ ($\sim 10.4 \text{ m}$, Figure 3a). Shallower than $\sim 10 \text{ m}$ the model substantially under-predicts water mass transformation, demonstrating that the shallow anti-clockwise lateral cell and the laterally spreading, turbulent pool contribute significantly to the transformation processes; features absent in the plume model. There is substantial uncertainty on the appropriate plume-ice drag coefficient to use in plume models (Jackson et al., 2020; Schulz et al., 2022). The model was therefore run with a conventional $C_d = 0.0025$ and again with $C_d = 0.015$ (Zhao et al., 2024), the latter resulting in an approximate doubling of the melt and a negligible ($\sim 2\%$) effect on vertical transports.

Modeled vertical plume heat transport and glacier melt-rate are computed. Vertical heat transport, $H_{BP} = 104 \times 10^7 \text{ W}$ (referenced to the freezing point), and the melt rate $Q_{M-\text{plume}} = 0.07$ to $0.16 \text{ m}^3 \text{ s}^{-1}$ depending on the drag coefficient. The heating rate required to achieve this melt rate is $H_{\text{PlumeMelt}} = 2.3$ to $5.4 \times 10^7 \text{ W}$, or 2%–5% of H_{BP} . By implication, 95%–98% of the vertical heat flux of the

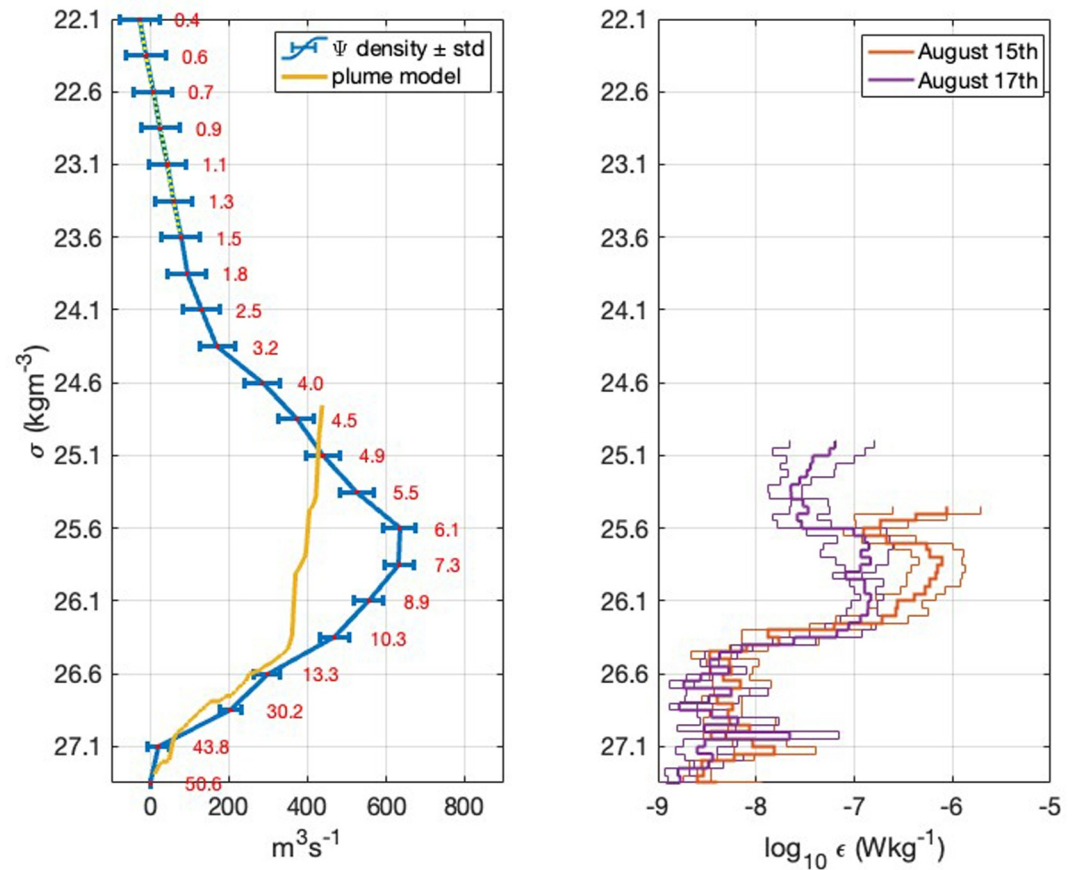


Figure 3. Section A. (a) Overturning stream function plotted against σ_θ on 16 August (blue line). Red numbers indicate the section-averaged depth of each isopycnal. Transformation according to buoyant plume theory (yellow line). Extrapolate region in green dashed; (b) TKE dissipation rate (ϵ) in σ_θ space from MSS profiles on 15 and 17 August. ϵ profile begin at ~ 4 m after sonde has reached a steady fall speed.

modeled plume is exported away from the glacier with 2%–5% used to melt glacial ice adjacent to the plume. Alternatively, the modeled plume melt $Q_{M_plume} = 0.07$ to 0.16 m³ s⁻¹ is 1.4%–3.3% of the total observationally estimated submarine melt $Q_M = 4.9 \pm 1.6$ m³ s⁻¹. The difference in percentages is within the error estimate of Q_M . In summary, the BP model accounts for $\sim 65\%$ of the vertical overturning within the fjord, but only 2%–5% of overall ice melt.

3.4. Sections B and C

ASV-based CTD and turbidity data show striking contrasts in between Sections B and C (Figure 4). On Section C isopycnal surfaces are relatively flat. Cold, less-turbid waters dominate the upper 10 m. Below that ($\sigma_\theta = 26.4 - 25$) warm, turbid water is seen >150 m horizontally from the glacier. In contrast, on Section B relatively warm, highly turbid water is continuously present between $\sigma_\theta = 24.0$ and 26.4 , and isopycnal surfaces dip and then rise dramatically between range 0–50 m. A Froude Number (F_r) for the spreading plume pool is formed from the ratio of the flow speed to the fastest internal wave phase speed $c_i = 0.27$ m s⁻¹ (see Supporting Information S1). Within a few 10 s of meters of the upwelling zone the ASV-derived horizontal flow speed exceeded 2 m s⁻¹, and on Section A the maximum flow speed was 0.3 m s⁻¹. Thus, the plume pool transitions from a thin, fast flowing layer ($F_r > 5.9$) to a slower, thicker layer ($F_r \leq 0.9$) as range-from-glacier increases; indicative of an internal hydraulic jump (Inall et al., 2005). Vertical mixing with water from below within the transition increases plume pool density, which then subducts sub-surface at ~ 100 m from the glacier (Figure 4). Beyond the transition, waters of the plume pool cool substantially and freshen slightly as range-from-glacier increases (Figure S3 in Supporting Information S1). Conversely, waters on Section C become warmer and

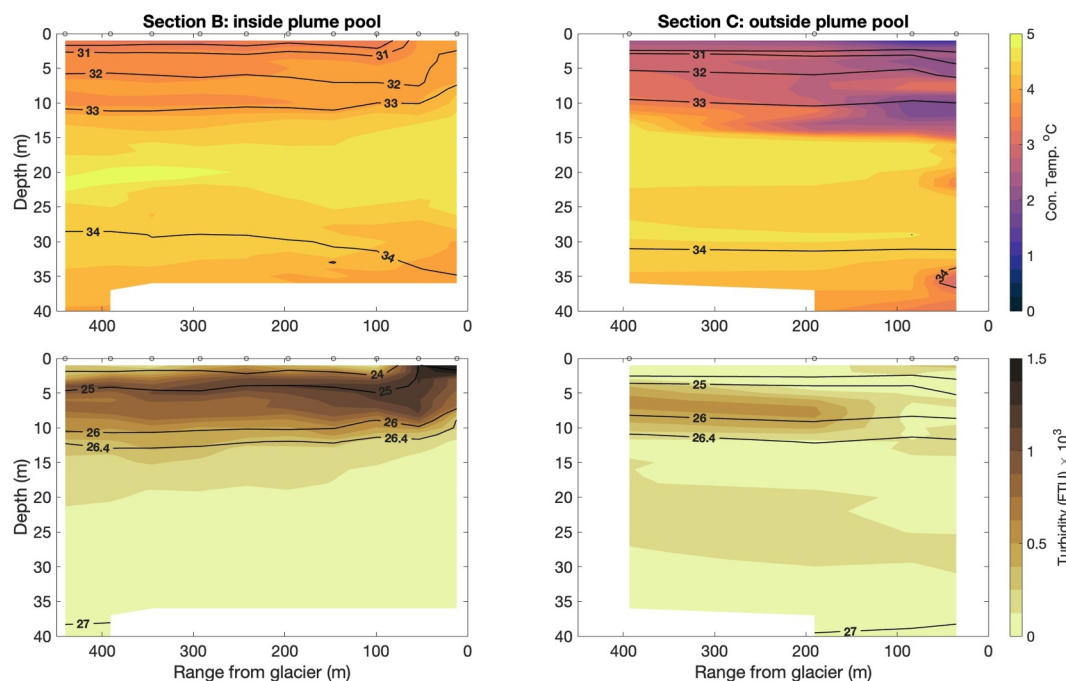


Figure 4. Autonomous Surface Vehicle Conductivity, Temperature, Depth Section B inside plume pool (left) and C outside plume pool (right), identified with blue and red markers, respectively on Figure 1. Colors show conservative temperature with salinity line contours (upper panels) and colors show turbidity (lower panels) with σ_θ line contours.

saltier as range increases. Horizontal interleaving of water masses is particularly apparent in the Section C temperature field and horizontal eddies with length scales ~ 6 m are visible on the surface (Figure 1e). A two end-member TS mixing model applied to TS properties on isopycnal $\sigma_\theta = 26.2$ on Sections B and C indicates that $\sim 50\%$ of the water nearest to the glacier on Section C is interleaved from Section B. Similarly, at range = 400 m, $\sim 40\%$ of Section B waters (on $\sigma_\theta = 26.2$) are comprised of Section C waters. The overall picture is of a turbulent, horizontally spreading supercritical jet, transitioning into a subcritical plume pool, rich in ~ 6 m scale eddy features, mixing horizontally with cool, fresh ambient-melt water.

We now compare vertical and horizontal heat exchange of the plume pool with the surrounding waters. Vertical heat fluxes within the plume pool at the intersection of Sections A and B are calculated from MSS90 profiles of T and ϵ using standard methodology (Sundfjord et al., 2007) (see Supporting Information S1). Large vertical fluxes are associated with the plume pool, with maxima of up to -400 W m^{-2} on $\sigma_\theta = 26.25$. Since temperature increases monotonically with depth, the turbid, spreading layer between $\sigma_\theta = 26.4$ and 25.5 on Section B is simultaneously heated from below and cooled from above; the difference results in a net heating $+182 \text{ W m}^{-2}$. The paradoxical cooling of the spreading layer as range-from-glacier increases (Figure S3 in Supporting Information S1) can only arise through horizontal entrainment of cooler ambient melt water, that is, horizontal eddy cooling outcompeting the net turbulent vertical warming. Applying a simple advection/diffusion model to a vertically homogeneous, radially spreading slab (see Supporting Information S1) gives a horizontal eddy diffusivity $K_H = 6.4 \pm 2.0 \text{ m}^2 \text{ s}^{-1}$ with a horizontal heat transport out of the plume pool of $1.2 \times 10^9 \pm 4.2 \times 10^8 \text{ W}$ required to account for the observed cooling of the spreading plume pool.

4. Discussion and Conclusion

Observations of horizontally spreading plume pools at distances of 500 m to 2 km from a glacial terminus are “limited” (Jackson et al., 2017). The focus here has been on quantifying the circulatory and mixing regime at distances ≤ 500 m in the presence of vigorous subglacial discharge; a region noted for a complete absence of direct mixing observations (Jackson et al., 2017). We demonstrate that this region, though stratified, is highly turbulent, with the plume pool entraining from above, below, and laterally (Figure 5). These findings help explain why observed estimates of observed export flux made at distances > 500 m from a terminus invariably exceed BP

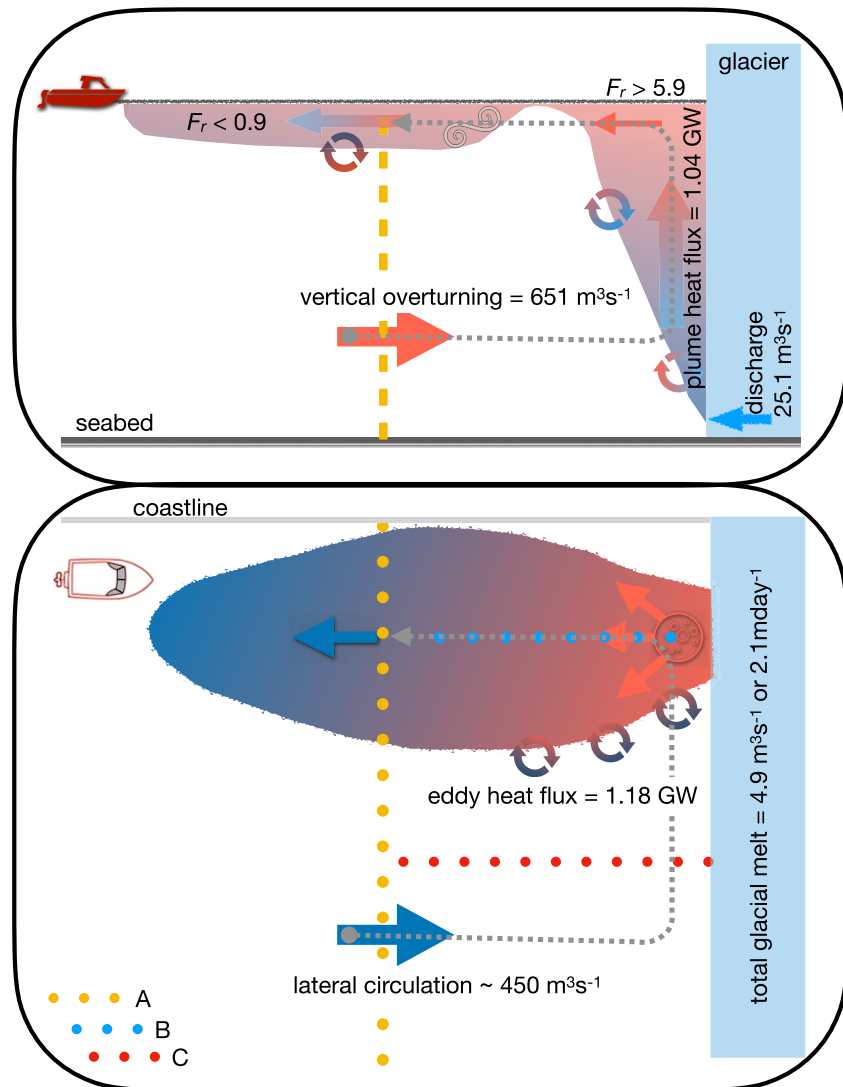


Figure 5. Schematics in x - z and x - y planes showing volume transports in the near-glacial zone. Arrows indicate flow, colored by temperature from warmest to coldest through red, orange, and blue. Plume and plume pool extent indicated with dashed black line, observational Sections A–C as indicated. All values are quoted in the main text and derived in Supporting Information S1.

theory estimates (Beaird et al., 2018; Muilwijk et al., 2022; Slater et al., 2022) which accounts only for entrainment into a vertically rising BP.

Peak vertical turbulent heat fluxes are large (400 W m^{-2}), 10 times reported values 10 s km away from the glacial terminus in a SE Greenland fjord (Inall et al., 2014). Assuming the observed vertical heat flux operates uniformly over a semi-circular area radius 500 m from the glacier, then the total vertical flux would be $\sim 16 \times 10^7 \text{ W}$, about 10% of the total vertical heat transport of the modeled rising plume. It is difficult to assess the accuracy of such an estimate, but it is likely a lower bound, since turbulent fluxes are evaluated at 500 m range, and no mixing estimates are available closer to the turbulent internal hydraulic jump. Other mechanisms which may be responsible for the observed elevated turbulence within the plume pool include both remnant turbulence from the rising plume and new turbulence production from internal waves, observed in coastal freshwater discharge from rivers (Nash & Moum, 2005), fjords (Toberman et al., 2017) and most recently in a plume pool (Cusack et al., 2023).

Modeled vertical heat transport within the plume ($H_{BP} \sim 104 \times 10^7 \text{ W}$) is similar in size to the horizontal heat transport out of the plume pool ($H_{H_pool} \sim 118 \times 10^7 \text{ W}$) whilst heat used in plume-induced melting is almost

two orders of magnitude lower ($H_{\text{PlumeMelt}} = 2.3 \text{ to } 5.4 \times 10^7 \text{ W}$). Thus, most of the heat entrained into the modeled BP is redirected into the outflowing plume pool. Within only $\sim 500 \text{ m}$ of the glacier, however, a great proportion of that heat is then mixed horizontally, cooling the plume pool whilst warming adjacent waters within 500 m of the glacial terminus. There are considerable uncertainties in estimates H_{BP} and $H_{\text{H_pool}}$ but the emergent picture is that horizontal mixing of warm plume pool waters is a dominant heat transport term within $\sim 500 \text{ m}$ of the glacier, consistent with notion that localized plumes drive horizontal movement all along a glacial terminus (Slater et al., 2018).

In terms of volume fluxes, modeled BP entrainment accounts for $\sim 65\%$ the observed vertical overturning, with entrainment into the plume pool providing the remainder. In terms of heat available to melt the glacier at the location of a rising plume; plume melt $Q_{M_plume} = 0.07 \text{ to } 0.16 \text{ m}^3 \text{ s}^{-1}$ is only a few percent (1.4%–3.3%) of the total submarine melt $Q_M = 4.9 \pm 1.6 \text{ m}^3 \text{ s}^{-1}$, which comprises both glacial front melt and iceberg melt in the control volume. This finding is consistent with other fjords in Alaska (Jackson et al., 2020, 2022) and in Greenland (Slater et al., 2018) where BPs account for a very small fraction of the total melt.

Finally, conventional wisdom on spreading gravity currents based on laboratory studies (Britter & Simpson, 1978) holds that entrainment in spreading gravity currents is insignificant other than that at the leading head. This is not the case here, vertical and horizontal entrainment are shown to be order one processes between the plume pool and the surrounding environment, adding quantitative evidence to the view that secondary effects of subglacial discharge plumes can dominate the terminus melting regime (Jackson et al., 2020, 2022; Slater et al., 2018) and supporting numerical and theoretical advances on the turbulent regime adjacent to MTGs (McConnochie et al., 2020).

Data Availability Statement

CTD and ADCP data from SAMS archive (Inall, 2023), MSS data from npolar archive (Sundfjord et al., 2024), Sentinel-2 RGB layers (Copernicus, 2023) processed using SNAP (ESA, 2023). Analysis and Figures 2 and 4 using Matlab R23b <https://uk.mathworks.com/products/matlab.html>. Figure 1 using QGIS <https://download.qgis.org/downloads/macOS/>. Figure 5 using Keynote <https://www.apple.com/uk/keynote/>.

Acknowledgments

Fram Centre Fjord & Coast flagship program and the Research Council of Norway through the project “Fjordic Freshwater Fluxes: Impacts on circulation and marine ecosystems” (Project No.: 328146). Ceslav Czyz, NPI Drone pilot. Adrian Perkins, Maritime Robotics. ASV support. DAS acknowledges support from NERC Independent Research Fellowship NE/T011920/1. MEI and DAS UKRI grant Fjordmix NE/W00531X/1. Three anonymous reviewers led to significant improvements in this manuscript.

References

- Beard, N. L., Straneo, F., & Jenkins, W. (2018). Export of strongly diluted Greenland meltwater from a major glacial fjord. *Geophysical Research Letters*, *45*(9), 4163–4170. <https://doi.org/10.1029/2018GL077000>
- Bendtsen, J., Mortensen, J., Lennert, K., & Rysgaard, S. (2015). Heat sources for glacial ice melt in a west Greenland tidewater outlet glacier fjord: The role of subglacial freshwater discharge. *Geophysical Research Letters*, *42*(10), 4089–4095. <https://doi.org/10.1002/2015GL063846>
- Britter, R. E., & Simpson, J. E. (1978). Experiments on the dynamics of a gravity current head. *Journal of Fluid Mechanics*, *88*(2), 223–240. <https://doi.org/10.1017/S0022112078002074>
- Carroll, D., Sutherland, D. A., Shroyer, E. L., Nash, J. D., Catania, G. A., & Stearns, L. A. (2017). Subglacial discharge-driven renewal of tidewater glacier fjords. *Journal of Geophysical Research*, *122*(8), 6611–6629. <https://doi.org/10.1002/2017JC012962>
- Copernicus. (2023). Copernicus data space ecosystem [Dataset]. *Programme of the European Union*. Retrieved from <https://dataspace.copernicus.eu/explore-data/data-collections/sentinel-data/sentinel-2>
- Cusack, J. M., Jackson, R. H., Nash, J. D., Skillingstad, E., Pettit, E. C., Sutherland, D. A., et al. (2023). Internal gravity waves generated by subglacial discharge: Implications for tidewater glacier melt. *Geophysical Research Letters*, *50*(12), e2022GL102426. <https://doi.org/10.1029/2022GL102426>
- Davison, B. J., Sole, A. J., Cowton, T. R., Lea, J. M., Slater, D. A., Fahrner, D., & Nienow, P. W. (2020). Subglacial drainage evolution modulates seasonal ice flow variability of three tidewater glaciers in southwest Greenland. *Journal of Geophysical Research: Earth Surface*, *125*(9), e2019JF005492. <https://doi.org/10.1029/2019JF005492>
- ESA. (2023). Science toolbox exploitation platform, SNAP V9.0.0 [Software]. *European Space Agency*. Retrieved from <https://step.esa.int/main/download/snap-download/previous-versions/>
- Howe, J. A. J. A., Husum, K., Inall, M. E., Coogan, J., Luckman, A., Arosio, R., et al. (2019). Autonomous underwater vehicle (AUV) observations of recent tidewater glacier retreat, western Svalbard. *Marine Geology*, *417*, 106009. <https://doi.org/10.1016/j.margeo.2019.106009>
- Inall, M. E. (2023). 2023GL104511_Archive [Dataset]. *SAMS*. Retrieved from https://thredds.sams.ac.uk/thredds/fileServer/FjordMixData/2023GL104511_Archive.tar.gz
- Inall, M. E., Murray, T., Cottier, F. R., Scharrer, K., Boyd, T. J., Heywood, K. J., & Bevan, S. L. (2014). Oceanic heat delivery via Kangerdlugssuaq Fjord to the South-East Greenland ice sheet. *Journal of Geophysical Research*, *119*(2), 631–645. <https://doi.org/10.1002/2013JC009295>
- Inall, M. E., Rippeth, T., Griffiths, C., & Wiles, P. (2005). Evolution and distribution of TKE production and dissipation within stratified flow over topography. *Geophysical Research Letters*, *32*(8), L08607. <https://doi.org/10.1029/2004gl022289>
- Jackson, R. H., Motyka, R. J., Amundson, J. M., Abib, N., Sutherland, D. A., Nash, J. D., & Kienholz, C. (2022). The relationship between submarine melt and subglacial discharge from observations at a tidewater glacier. *Journal of Geophysical Research: Oceans*, *127*(10), e2021JC018204. <https://doi.org/10.1029/2021JC018204>

- Jackson, R. H., Nash, J. D., Kienholz, C., Sutherland, D. A., Amundson, J. M., Motyka, R. J., et al. (2020). Meltwater intrusions reveal mechanisms for rapid submarine melt at a tidewater glacier. *Geophysical Research Letters*, *47*(2), e2019GL085335. <https://doi.org/10.1029/2019GL085335>
- Jackson, R. H., Shroyer, E. L., Nash, J. D., Sutherland, D. A., Carroll, D., Fried, M. J., et al. (2017). Near-glacier surveying of a subglacial discharge plume: Implications for plume parameterizations. *Geophysical Research Letters*, *44*(13), 6886–6894. <https://doi.org/10.1002/2017GL073602>
- Jackson, R. H., & Straneo, F. (2016). Heat, salt, and freshwater budgets for a glacial fjord in Greenland. *Journal of Physical Oceanography*, *46*(9), 2735–2768. <https://doi.org/10.1175/JPO-D-15-0134.1>
- Kneib-Walter, A., Lüthi, M. P., Moreau, L., & Vieli, A. (2021). Drivers of recurring seasonal cycle of glacier calving styles and patterns. *Frontiers in Earth Science*, *9*, 667717. <https://doi.org/10.3389/feart.2021.667717>
- Lindbäck, K., Kohler, J., Pettersson, R., Nuth, C., Langley, K., Messerli, A., et al. (2018). Subglacial topography, ice thickness, and bathymetry of Kongsfjorden, northwestern Svalbard. *Earth System Science Data*, *10*(4), 1769–1781. <https://doi.org/10.5194/essd-10-1769-2018>
- Luckman, A., Benn, D. I., Cottier, F., Bevan, S., Nilsen, F., & Inall, M. (2015). Calving rates at tidewater glaciers vary strongly with ocean temperature. *Nature Communications*, *6*(1), 8566. <https://doi.org/10.1038/ncomms9566>
- Mankoff, K. D., Straneo, F., Cenedese, C., Das, S. B., Richards, C. G., & Singh, H. (2016). Structure and dynamics of a subglacial discharge plume in a Greenlandic fjord. *Journal of Geophysical Research: Oceans*, *121*(12), 8670–8688. <https://doi.org/10.1002/2016JC011764>
- McConnochie, C. D., Cenedese, C., & McElwaine, J. N. (2020). Surface expression of a wall fountain: Application to subglacial discharge plumes. *Journal of Physical Oceanography*, *50*(5), 1245–1263. <https://doi.org/10.1175/JPO-D-19-0213.1>
- Moyer, A. N., Sutherland, D. A., Nienow, P. W., & Sole, A. J. (2019). Seasonal variations in iceberg freshwater flux in Sermilik fjord, southeast Greenland from Sentinel-2 imagery. *Geophysical Research Letters*, *46*(15), 8903–8912. <https://doi.org/10.1029/2019GL082309>
- Muillwijk, M., Straneo, F., Slater, D. A., Smedsrud, L. H., Holte, J., Wood, M., et al. (2022). Export of ice sheet meltwater from Upernavik fjord, west Greenland. *Journal of Physical Oceanography*, *52*(3), 363–382. <https://doi.org/10.1175/JPO-D-21-0084.1>
- Murray, T., Scharrer, K., James, T. D., Dye, S. R., Hanna, E., Booth, A. D., et al. (2010). Ocean regulation hypothesis for glacier dynamics in southeast Greenland and implications for ice sheet mass changes. *Journal of Geophysical Research*, *115*(F3), F03026. <https://doi.org/10.1029/2009JF001522>
- Nash, J. D., & Moum, J. N. (2005). River plumes as a source of large-amplitude internal waves in the coastal ocean. *Nature*, *437*(7057), 400–403. <https://doi.org/10.1038/nature03936>
- Prandke, H., & Stipps, A. (1998). A microstructure profiler to study mixing and turbulent transport processes. In *IEEE oceans 1998* (Vol. 1, pp. 179–183).
- Schulz, K., Nguyen, A. T., & Pillar, H. R. (2022). An improved and observationally-constrained melt rate parameterization for vertical ice fronts of marine terminating glaciers. *Geophysical Research Letters*, *49*(18), e2022GL100654. <https://doi.org/10.1029/2022GL100654>
- Slater, D. A., Carroll, D., Oliver, H., Hopwood, M. J., Straneo, F., Wood, M., et al. (2022). Characteristic depths, fluxes, and timescales for Greenland's tidewater glacier fjords from subglacial discharge-driven upwelling during summer. *Geophysical Research Letters*, *49*(10), e2021GL097081. <https://doi.org/10.1029/2021GL097081>
- Slater, D. A., Goldberg, D. N., Nienow, P. W., & Cowton, T. R. (2016). Scalings for submarine melting at tidewater glaciers from buoyant plume theory. *Journal of Physical Oceanography*, *46*(6), 1839–1855. <https://doi.org/10.1175/JPO-D-15-0132.1>
- Slater, D. A., Straneo, F., Das, S. B., Richards, C. G., Wagner, T. J. W., & Nienow, P. W. (2018). Localized plumes drive front-wide ocean melting of a Greenlandic tidewater glacier. *Geophysical Research Letters*, *45*(22), 12350–12358. <https://doi.org/10.1029/2018GL080763>
- Sundfjord, A., Albrechtsen, J., Kasajima, Y., Skogseth, R., Kohler, J., Nuth, C., et al. (2017). Effects of glacier runoff and wind on surface layer dynamics and Atlantic Water exchange in Kongsfjorden, Svalbard; a model study. *Estuarine, Coastal and Shelf Science*, *187*, 260–272. <https://doi.org/10.1016/j.ecss.2017.01.015>
- Sundfjord, A., Czyz, C., Coogan, J., & Inall, M. (2024). Microstructure profiler (MSS) profiles from Kongsfjorden 2021 [Dataset]. *Norwegian Polar Institute*. <https://doi.org/10.21334/npolar.2024.d2a4f5c8>
- Sundfjord, A., Fer, I., Kasajima, Y., & Svendsen, H. (2007). Observations of turbulent mixing and hydrography in the marginal ice zone of the Barents Sea. *Journal of Geophysical Research*, *112*(C5), 121. <https://doi.org/10.1029/2006JC003524>
- Sutherland, D. A., Jackson, R. H., Kienholz, C., Amundson, J. M., Dryer, W. P., Duncan, D., et al. (2019). Direct observations of submarine melt and subsurface geometry at a tidewater glacier. *Science*, *365*(6451), 369–374. <https://doi.org/10.1126/science.aax3528>
- Svendsen, H., Beszczynska-Møller, A., Hagen, J. O., Lefaconnier, B., Tverberg, V., Gerland, S., et al. (2002). The physical environment of Kongsfjorden-Krossfjorden, an Arctic fjord system in Svalbard. *Polar Research*, *21*(1), 133–166. <https://doi.org/10.1111/j.1751-8369.2002.tb00072.x>
- Toberman, M., Inall, M. E., Boyd, T., Dumont, E., & Griffiths, C. (2017). AUV and time-lapse photography observations of buoyant plumes and non-linear internal waves generated by sea loch outflow. *Journal of Geophysical Research*, *122*(7), 5522–5544. <https://doi.org/10.1002/2016JC012208>
- Tverberg, V., Skogseth, R., Cottier, F., Sundfjord, A., Walczowski, W., Inall, M. E., et al. (2019). The Kongsfjorden transect: Seasonal and inter-annual variability in hydrography. In *The Ecosystem of Kongsfjorden, Svalbard* (pp. 49–104). https://doi.org/10.1007/978-3-319-46425-1_3
- Zhao, K. X., Skyllingstad, E. D., & Nash, J. D. (2024). Improved parameterizations of vertical ice-ocean boundary layers and melt rates. *Geophysical Research Letters*, *51*(4), e2023GL105862. <https://doi.org/10.1029/2023GL105862>
- Zhao, K. X., Stewart, A. L., & McWilliams, J. C. (2021). Geometric constraints on glacial fjord–shelf exchange. *Journal of Physical Oceanography*, *51*(4), 1223–1246. <https://doi.org/10.1175/JPO-D-20-0091.1>
- Zhao, K. X., Stewart, A. L., & McWilliams, J. C. (2022). Linking overturning, recirculation, and melt in glacial fjords. *Geophysical Research Letters*, *49*(15), e2021GL095706. <https://doi.org/10.1029/2021GL095706>

References From the Supporting Information

- Taylor, G. I. (1931). Effect of variation in density on the stability of superposed streams of Fluid. *Proceedings of the Royal Society of London Series A: Containing Papers of a Mathematical and Physical Character*, *132*(820), 499–523. <https://doi.org/10.1098/rspa.1931.0115>